Development of an Upwinding Particle Interaction Kernel for Simulating Incompressible Navier-Stokes Equations

Chinlong Huang,[1] **Tony W. H. Sheu**[1,2,3]

[1] *Department of Engineering Science and Ocean Engineering, National Taiwan University, 10617 Taipei, Taiwan*

[2] *Taida Institute of Mathematical Science (TIMS), National Taiwan University, 10617 Taipei, Taiwan*

[3] *Center for Quantum Science and Engineering (CQSE), National Taiwan University, 10617 Taipei, Taiwan*

In this study, we are aimed to derive a kernel function, which accounts for the interaction among particles, within the framework of particle method. To get a computationally more accurate solution for the incompressible Navier-Stokes equations, determination of kernel function is a key to success in the developed interaction model. In the light of the underlying fact that the smoothed quantity for a scalar or a vector at a particle location is mathematically identical to its collocated value provided that the kernel function is chosen as the Dirac delta function, our guideline is to make the modified kernel function closer to the Dirac delta function as much as possible in flow conditions when diffusion dominates convection. As convection prevailingly dominates its diffusion counterpart, particle interaction at the upstream side should be favorably taken into account to avoid numerical oscillations resulting from the convective instability. The proposed particle interaction model featuring with the newly developed kernel function will be validated through several scalar transport and Navier-Stokes problems which have either analytical or benchmark solutions. The stability condition and the spatial accuracy order of the proposed particle interaction model will be also analyzed in details in this article for the sake of completeness.   © 2011 Wiley Periodicals, Inc. Numer Methods Partial Differential Eq 28: 1574–1597, 2012

Correspondence to: Tony W. H. Sheu, No. 1, Sec. 4, Roosevelt Road, Taipei 10617, Taiwan (e-mail: twhsheu@ntu.edu.tw)

I. INTRODUCTION

Techniques available for solving the flow equations can be divided into the Eulerian and Lagrangian formulation types. In the Eulerian class of methods, the governing equations are solved at a fixed mesh system. In Lagrangian methods, which can be subdivided into the mesh and meshfree two subgroups, the generated mesh points are not fixed in the domain but will be advected with the flow field. As a result, Lagrangian methods have an apparent advantage of simulating flow equations as we have no need to approximate the convection terms shown in the transport equations. In the literature, another mathematically rigorous arbitrary Lagrangian-Eulerian method [1] employs both Lagrangian and Eulerian solution steps in the course of changing the meshes with time.

Besides the well-known grid-based methods, such as the marker-and-cell [2], volume-of-fluid [3], and level-set [4] methods, that have been successfully applied to predict free surface flows, there existed another major class of meshfree methods known as the particle methods. Particle methods are featured with the prescribed particles moving in a Lagrangian sense such that the convection terms can be directly calculated from the motion of particles without incurring any numerical diffusion. Particle methods can be also separated into the Eulerian particle method, such as the particle-in-cell method [5] and the Lagrangian particle methods, which include the well-known smoothed particle hydrodynamics (SPH) and the moving particle semi-implicit (MPS) methods. SPH method, introduced firstly by Lucy [6] and Gingold and Monaghan [7] at about the same time, was developed for the simulation of compressible fluid flows based on the inter-polation theory through the introduced kernel function (or smoothing kernel). SPH method was later extended to simulate the incompressible free surface flow [8].

In MPS method developed to simulate the incompressible Navier-Stokes fluid flows [9], the motion of each particle is calculated through the interaction with its neighboring particles by means of the kernel (or weight) function. This means that all the spatial derivatives can be approximated by the deterministic particle interaction without the need of generating a mesh in the flow domain. This explains why MPS method has gradually become very effective for use in simulating many practical problems which have either complicated geometry or complex physics. For the problems with the inflow–outflow boundaries, this method was however found to have the difficulty to trace fluid particles easily. In addition, MPS method requires extra computational time to find all neighboring points. One point worthy to address here is that the power of Graphic Process Unit, which has been recently implemented to accelerate many nongraphic calculations, has not been fully explored mainly because of the inefficient search of the neighbors in particle-based methods [10].

While MPS method has been proposed more than a decade to simulate the low-speed complex flow physics with great success, its computational insight has been comparatively less explored. Questions about the deteriorated solution accuracy in some cases with the increasingly refined mesh and the slow convergence of solution for the calculation carried out at a slightly higher Peclet number have been often raised. For this reason, we will simplify the analysis in this study by considering first the stationary particle method to get some theoretical insights through a rigorous analysis of the proposed particle method.

The rest of this article will be organized as follows. In Section II, we will present the Navier-Stokes and passive scalar equations, which involve both of the convection and diffusion flux terms. This is followed by presenting the particle interaction model for approximating the gradient and Laplacian differential operators. We will address in Section IV the kernel function that is needed in the particle method. In Section V, we will validate the proposed particle model by solving the convection-diffusion equation that is amenable to the analytic solution. Problems involving

the smoothly varying interior layer and the boundary layer solutions will be also investigated for the validation sake. In the final section, some conclusions will be drawn based on the predicted results.

II. WORKING EQUATION

We will consider in this study the following Navier-Stokes equations in a simply connected domain Ω for modeling the motion of an incompressible fluid flow.

$$u\frac{\partial u}{\partial x} + v\frac{\partial u}{\partial y} = -\frac{\partial p}{\partial x} + \frac{\partial}{\partial x}\left(\frac{1}{Re}\frac{\partial u}{\partial x}\right) + \frac{\partial}{\partial y}\left(\frac{1}{Re}\frac{\partial u}{\partial y}\right) \tag{1}$$

$$u\frac{\partial v}{\partial x} + v\frac{\partial v}{\partial y} = -\frac{\partial p}{\partial y} + \frac{\partial}{\partial x}\left(\frac{1}{Re}\frac{\partial v}{\partial x}\right) + \frac{\partial}{\partial y}\left(\frac{1}{Re}\frac{\partial v}{\partial y}\right) \tag{2}$$

$$\frac{\partial u}{\partial x} + \frac{\partial v}{\partial y} = 0 \tag{3}$$

In Eqs. (1) and (2), $Re = \frac{UL}{\nu}$ stands for the Reynolds number, where L is the characteristic length, U is the reference velocity, and ν is the kinematic viscosity.

The following model equation will be used to develop the kernel function because it is the key equation in the simulation of momentum equations for an incompressible fluid flow.

$$u\frac{\partial \phi}{\partial x} + v\frac{\partial \phi}{\partial y} = \mu\left(\frac{\partial^2 \phi}{\partial x^2} + \frac{\partial^2 \phi}{\partial y^2}\right) \tag{4}$$

Both of the velocity components u, v and viscosity μ in Eq. (4) are assumed to have the constant values to facilitate the following development of kernel function.

III. DETERMINISTIC PARTICLE INTERACTION MODELS FOR DIFFERENTIAL OPERATORS

It has been known for a long time that it is difficult to apply the grid-based methods to predict some viscous flow problems involving the multiphase, fluid mixing, and sedimentary. Particle-based methods, on the other hand, become gradually popular in the simulation of incompressible viscous fluid flows with either a free surface or an interface. In particle methods, the differential operators for the mass and momentum conservations shown in Section II need to be replaced by their corresponding particle interaction operators. In other words, partial differential equations will be transformed to their corresponding particle interaction equations so that the transport equation under investigation can be approximated by a finite number of moving or stationary particles and their interactions. The key to success is the chosen kernel (or weighting) function for the particles that are apart from each other by a user's prescribed finite distance.

Consider a particle, at which some of its physical quantities f_i are defined, at the location i. One can approximately represent f_i at a point $\underline{r}$ as follows by virtue of the kernel function $w(\underline{r})$

$$\langle f(\underline{r})\rangle \cdot \sum_i w(|\underline{r}_i - \underline{r}|) = \sum_i f_i w(|\underline{r}_i - \underline{r}|) \tag{5}$$

It is important to point out here that the smoothed quantity $\langle f \rangle_i$ at the particle location $\underline{r}_i$ turns out to be exactly identical to the local value f_i if the chosen kernel function is the Dirac delta function. This implies that the kernel function $w(\underline{r})$, which should be constrained by $\int_V w(r)dV = 1$, shown in (5) determines the prediction quality using the particle method. One can find different variants of the kernel function in [11].

For a scalar ϕ at a location $\underline{r}_j$, one can get its value by performing a Taylor series expansion of ϕ with respect to its value at $\underline{r}_i$ as follows:

$$\phi_j = \phi_i + \nabla\phi|_{ij} \cdot (\underline{r}_j - \underline{r}_i) + H.O.T. \tag{6}$$

By dropping the higher-order terms shown above, we can get the first-order approximated equation $\phi_j - \phi_i = \nabla\phi|_{ij} \cdot (\underline{r}_j - \underline{r}_i)$. By multiplying $(\underline{r}_j - \underline{r}_i)^{-1}$ on both hand sides of the above equation, the following gradient operator can be derived.

$$\nabla\phi|_{ij} = \frac{(\phi_j - \phi_i)(\underline{r}_j - \underline{r}_i)}{|\underline{r}_j - \underline{r}_i||\underline{r}_j - \underline{r}_i|} \tag{7}$$

Let $\nabla\phi|_{ij}$ be f and substitute it into Eq. (5), we can get the following smoothed representation of $\nabla\phi$, which is denoted by $\langle\nabla\phi\rangle$ at a node ij, in a d-dimensional space

$$\langle\nabla\phi\rangle|_{ij} = \frac{d}{n^0} \sum_{j\neq i} \frac{\phi_j - \phi_i}{|\underline{r}_j - \underline{r}_i|}(\underline{r}_j - \underline{r}_i)w(\underline{r}_j - \underline{r}_i) \tag{8}$$

In the above equation, n^0 denotes the particle number density and it is defined as $\sum_{j\neq i} w(|\underline{r}_j - \underline{r}_i|)$. Under the incompressible flow condition, $n_i = n^0$ will be used in the current flow simulation.

One can similarly derive the following Laplacian operator for a scalar function ϕ, which has been derived before in [9]

$$\langle\nabla^2\phi\rangle|_i = \frac{2d}{\lambda n^0} \sum_{j\neq i}(\phi_j - \phi_i)w(|\underline{r}_j - \underline{r}_i|) \tag{9}$$

where

$$\lambda = \frac{\int_{V'} |\underline{r}_j - \underline{r}_i|^2 w(|\underline{r}_j - \underline{r}_i|)dV}{\int_{V'} w(|\underline{r}_j - \underline{r}_i|)dV} \tag{10}$$

Note that V' is the volume excluding of a small interval that includes a point at $\underline{r}_i$. Another smoothed Laplacian operator $\langle\nabla^2\phi\rangle_i$ has been derived as follows from the divergence of $\nabla\phi$ [12]

$$\langle\nabla^2\phi\rangle|_{ij} = \frac{2d}{n^0} \sum_{j\neq i} \frac{\phi_j - \phi_i}{|\underline{r}_j - \underline{r}_i|}w(|\underline{r}_j - \underline{r}_i|) \tag{11}$$

The advantage of employing particle methods becomes clear in that all of the spatial derivative terms can be calculated from the chosen kernel function without invoking grids. Considerable effort in the generation of good-quality meshes for the numerical simulation in a stationary or in a moving domain is therefore avoided.

Unlike the SPH particle method, calculations of $\nabla\phi$ and $\nabla^2\phi$ in Eqs. (8)–(9), and (11) involve only the kernel function $w(\underline{r})$ itself. As the derivative of kernel function needs not to be calculated in the approximation of these two differential operators, numerical oscillations, which may be generated in the traditional fixed grid Eulerian approach for the cases involving high solution gradients, can be completely avoided. As a result, one can have a greater flexibility to choose proper kernel function that has a slope as steep as the Dirac delta function.

IV. DEVELOPMENT OF THE KERNEL FUNCTIONS

Owing to Eqs. (8) and (9)–(11), we know that the quality of the approximated operators $\langle \nabla \phi \rangle_{ij}$ and $\langle \nabla^2 \phi \rangle_i$ depends entirely on the chosen kernel function $w(r)$ and the number of the prescribed particles, which will affect r_i. Moreover, the chosen particle locations and kernel function will determine the subsequent particle locations using the moving particle methods. The prediction quality depends therefore highly on the chosen kernel function, which will be derived below in detail.

In the light of Eq. (5), the Dirac delta function $\delta(\underline{r})$, which is constrained by $\int_{-\infty}^{\infty} \delta(\underline{r}) dr = 1$, is an ideal candidate for the kernel function. This kernel function is, unfortunately, not implementable in computational practice. We have therefore to resort to the smoothed Dirac delta function when carrying out simulations based on the particle method. The smoothed Dirac delta function is sometimes called as the nascent delta function $\delta_\varepsilon(\underline{r})$, which is defined as $\lim_{\varepsilon \to 0} \delta_\varepsilon(\underline{r}) = \delta(\underline{r})$. In the literature, several nascent delta functions, such as the Gaussian function, Lorentz line function, impulse function, and sinc function, can be found. There exists also a different class of kernel functions which were developed irrelevantly to the nascent delta functions. Typical examples include the exponential, cubic spline, and quadratic spline functions proposed by Belytschko et al. [13] and the kernel functions proposed by Koshizuka and Oka in 1996 [14] and Koshizuka et al. in 1998 [15].

A. Center-Type Kernel Function for the Pure Diffusion Equation

In this study, we intend to develop a new kernel function so that it can be rigorously applied to simulate the incompressible Navier-Stokes equations based on the particle methods. Our guidelines of developing the proposed kernel function will be given below. The kernel function $w(r)$ chosen in the current development falls into the category of the nascent delta function. This implies that $\lim_{r_e \to 0} w(\underline{r}, r_e) = \delta(\underline{r})$, where r_e is the radius of a small circle. The weight between any two arbitrary particles that are apart by a distance r will be forced to be zero as $r \geq r_e$. For the sake of accuracy, the kernel function will be developed to retain the following inherent feature

$$\int_{-\infty}^{\infty} w(\underline{r}, r_e) d\underline{r} = 1 \tag{12}$$

Development of the current kernel function starts with representing $w(\underline{r})$ in terms of the dimensionless length ratio $\frac{r}{r_e}$ as

$$w(r) = \begin{cases} \dfrac{a}{r_e} + \dfrac{b}{r_e} \left(\dfrac{r}{r_e} \right) + \dfrac{c}{r_e} \left(\dfrac{r}{r_e} \right)^2 + \dfrac{d}{r_e} \left(\dfrac{r}{r_e} \right)^3 + \dfrac{e}{r_e} \left(\dfrac{r}{r_e} \right)^4 ; & 0 \leq r \leq r_e \\ 0; & r_e < r \end{cases} \tag{13}$$

Derivation of $w(\underline{r})$ is followed by imposing the constraint conditions given by $w(r = r_e) = \frac{\partial w}{\partial r}\big|_{r=r_e} = \frac{\partial w}{\partial r}\big|_{r=0} = 0$ and $\int_0^{\frac{r}{r_e}=1} w(r) dr = \frac{1}{2}$. Imposition of the above four conditions enables us to get the algebraic equations given below

$$a + b + c + d + e = 0 \tag{14}$$

$$b + 2c + 3d + 4e = 0 \tag{15}$$

$$a + \frac{b}{2} + \frac{c}{3} + \frac{d}{4} + \frac{e}{5} = \frac{1}{2} \tag{16}$$

$$b = 0 \tag{17}$$

Having derived the above four algebraic equations, one can then easily express the free parameters a, b, c, and d in terms of e as $a = 1 - \frac{1}{15}e$, $b = 0$, $c = -3 + \frac{6}{5}e$, and $d = 2 - \frac{32}{15}e$.

By substituting the resulting kernel function into Eq. (11) for $\nabla^2 \phi$, the following discrete equation for $\frac{\partial^2 \phi}{\partial x^2} + \frac{\partial^2 \phi}{\partial y^2} = 0$ can be derived from the particle method

$$\frac{1}{[w(h) + 2w(\sqrt{2}h)]h^2}\{(\phi_{i+1,j} + \phi_{i-1,j} + \phi_{i,j+1} + \phi_{i,j-1} - 4\phi_i)w(h)$$

$$+ (\phi_{i+1,j+1} + \phi_{i-1,j+1} + \phi_{i+1,j-1} + \phi_{i-1,j-1} - 4\phi_i)w(\sqrt{2}h)\} = 0 \tag{18}$$

In the above equation, h denotes the grid size. The detailed derivation of the above equation is given in Appendix A. By performing the modified equation analysis on Eq. (18), we get the following modified equation

$$\frac{\partial^2 \phi}{\partial x^2} + \frac{\partial^2 \phi}{\partial y^2} = -\left[\frac{w(\sqrt{2}h)}{w(h) + 2w(\sqrt{2}h)}\frac{\partial^4 \phi}{\partial x^2 \partial y^2} + \frac{1}{12}\frac{\partial^4 \phi}{\partial x^4} + \frac{1}{12}\frac{\partial^4 \phi}{\partial y^4}\right]h^2$$

$$-\left[\frac{w(\sqrt{2}h)}{12(w(h) + 2w(\sqrt{2}h))}\left(\frac{\partial^6 \phi}{\partial x^4 \partial y^2} + \frac{\partial^6 \phi}{\partial x^2 \partial y^4}\right) + \frac{1}{360}\frac{\partial^6 \phi}{\partial x^6} + \frac{1}{360}\frac{\partial^6 \phi}{\partial y^6}\right]h^4 + \cdots \tag{19}$$

Let $w(\sqrt{2}h) = \frac{1}{4}w(h)$, the first term on the right-hand side of the above equation turns out to be zero due to $\frac{\partial^2 \phi}{\partial x^2} + \frac{\partial^2 \phi}{\partial y^2} = 0$.

Provided that $r_e = 2h$, we can easily know from the following nine-point stencil equation that the approximated equation for (4) investigated at $\mu = \infty$ has the accuracy order of fourth.

$$\frac{\phi_{i+1,j+1} + \phi_{i-1,j+1} + \phi_{i-1,j+1} + \phi_{i+1,j-1} + 4\phi_{i+1,j} + 4\phi_{i-1,j} + 4\phi_{i,j+1} + 4\phi_{i,j-1} - 20\phi_{i,j}}{6h^2}$$

$$+ O(h^4) = 0 \tag{20}$$

Note that Eq. (20) is derived under the condition given by

$$3a + \left(2\sqrt{2} - \frac{1}{2}\right)b + \left(2 - \frac{1}{4}\right)c + \left(\sqrt{2} - \frac{1}{8}\right)d + \left(1 - \frac{1}{16}\right)e = 0 \tag{21}$$

The resulting five free parameters can then be uniquely calculated from Eqs. (14)–(17) and (21) as $a = \frac{480\sqrt{2}-705}{512\sqrt{2}-745}$, $b = 0$, $c = \frac{-960\sqrt{2}+1515}{512\sqrt{2}-745}$, $d = \frac{-210}{512\sqrt{2}-745}$, $e = \frac{480\sqrt{2}-600}{512\sqrt{2}-745}$.

In summary, the kernel function developed for the prediction of a pure diffusion equation is as follows

$$
w(r) = \begin{cases} \dfrac{480\sqrt{2}-705}{512\sqrt{2}-745}\dfrac{1}{r_e} + \dfrac{-960\sqrt{2}+1515}{512\sqrt{2}-745}\dfrac{1}{r_e}\left(\dfrac{r}{r_e}\right)^2 \\ \quad + \dfrac{-210}{512\sqrt{2}-745}\dfrac{1}{r_e}\left(\dfrac{r}{r_e}\right)^3 + \dfrac{480\sqrt{2}-600}{512\sqrt{2}-745}\dfrac{1}{r_e}\left(\dfrac{r}{r_e}\right)^4 ; \quad 0 \le r \le r_e \\ 0; \hspace{7cm} r_e < r \end{cases}
\tag{22}
$$

Note that this kernel function is derived under the condition of

$$
w(\sqrt{2}h) = \frac{1}{4}w(h)
\tag{23}
$$

Unlike the kernel function $w(r) = \frac{r_e}{r} - 1$ proposed in [14], which approaches infinity as the value of r becomes zero, this newly developed kernel function has its maximum value at $r = 0$. It is also worthy to restate that the developed kernel function for solving the pure diffusion equation satisfies the following constraint condition, which is also embedded in the Dirac delta function

$$
\int_{\frac{r}{r_e}=-1}^{\frac{r}{r_e}=1} w(r)dr = 1
\tag{24}
$$

B. Upwind-Type Kernel Function for the Convection-Diffusion Equation

According to Fig. 1, which plots $w(r)$ shown in Eq. (22), we know that the kernel function developed within the framework of Dirac delta function can be used to get the center-type approximation as the particles distanced from the reference node with the same length will impose the same influence (or weight) on that reference node. Such an interaction model is applicable only to the diffusion dominant case (or $Pe(\equiv \frac{|u|h}{\mu}) < 2$), where h and μ denote the grid size and the fluid viscosity, respectively. In most of the science and practical engineering problems, the value of Peclet number Pe is much larger than two. Application of the kernel function developed in the previous subsection and other published kernel functions in [13–15] to simulate the practical flow problems may result in non-physical oscillations. To resolve this notorious convective instability problem, we must take the physics of fluid flow into consideration in the course of developing the kernel function in particle methods.

Our idea of suppressing oscillatory solutions generated by the convective instability is to implicitly add an appropriate amount of the damping along the flow direction. Consider a flow with a local velocity vector (u, v), the damping term ϕ_{ss} along its local tangential direction, which is $s(\equiv \tan^{-1}(\frac{v}{u}))$, given below is derived in Appendix B

$$
\phi_{ss} = \frac{u^2}{u^2 + v^2}\phi_{xx} + \frac{v^2}{u^2 + v^2}\phi_{yy} + \frac{2uv}{u^2 + v^2}\phi_{xy}
\tag{25}
$$

Thanks to the above relation, we know that the kernel function derived for the high Peclet number flow case must implicitly generate a sufficient amount of numerical dissipation along the streamline direction so as to stabilize the discrete equation in (4).

In this study, we will modify the kernel function (22) that has been developed for the simulation of low Peclet number flow equation by adding a stabilization term to the kernel function (22).
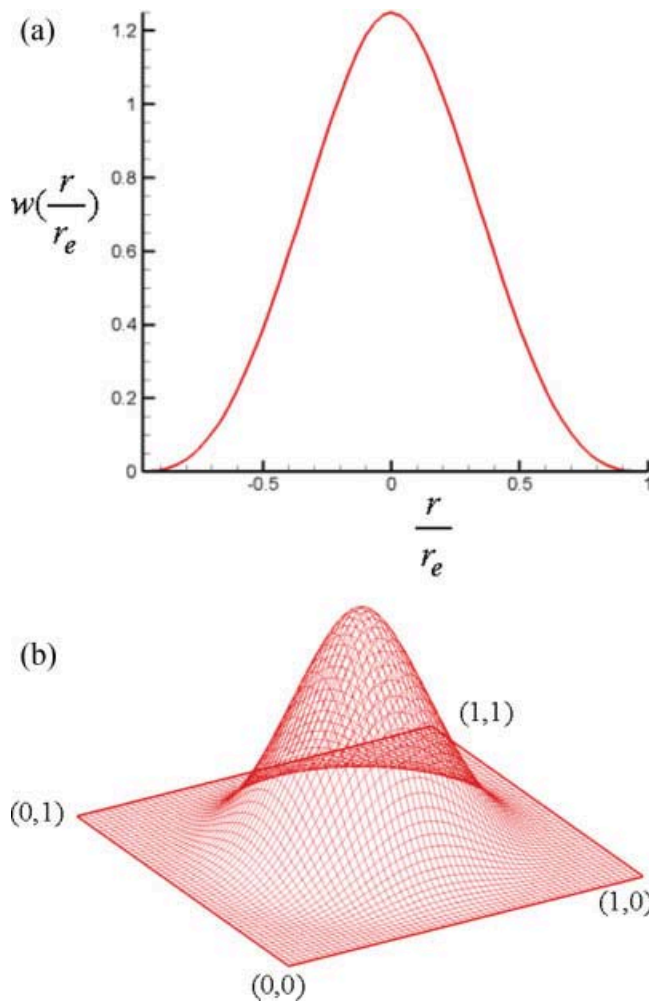
FIG. 1.   The plots of the center-type kernel function given in Eq. (22) for the Laplace equation. (a) Plotted in r/r_e-coordinate. (b) Plotted in xy plane. [Color figure can be viewed in the online issue, which is available at wileyonlinelibrary.com.]

For the stabilization sake, we need to change the center-type kernel function $w(r)$, which is given in (26), to its non-centered counterpart $W(r)$ by adding a term $B(r)$ that can bring the required numerical stabilization into the particle method. The upwinding-type kernel function is therefore proposed as follows

$$W(r) = w(r) + B(r) \qquad (26)$$

The stabilization kernel function B given below has a form similar to that used in the streamline upwind Petrov Galerkin finite element model [16, 17]

$$B(r) = \tau u^k|_i \frac{\partial w|_i}{\partial x^k} \qquad (27)$$

Numerical Methods for Partial Differential Equations DOI 10.1002/num

Inclusion of the velocity vector $\underline{u}$ and the gradient of kernel function can be shown to be able to render a second-order damping term ϕ_{ss} along the flow direction s. Note that the so-called crosswind diffusion term ϕ_{xy} is also introduced in this formulation. Owing to the inclusion of ϕ_{xy} in the approximation, we are motivated to develop a scheme that is as accurate as possible so that the false diffusion error can be reduced or even minimized. The consequence is that τ, which is known to determine the degree of upwinding, needs to be rigorously derived.

For the sake of accuracy, the upwinding coefficient τ shown in Eq. (27) will be developed in the limiting one-dimensional condition since the following equation is amenable to an exact solution.

$$u \frac{\partial \phi}{\partial x} = \mu \frac{\partial^2 \phi}{\partial x^2} \tag{28}$$

One can substitute Eqs. (8), (11), (22), and (26)–(27) into Eq. (28) to derive the following discrete equation at a node i

$$u \frac{\phi_{i+1} - \phi_{i-1}}{2h} - \mu \left(1 + \frac{\tau h u^2 w'(h)}{2\mu w(h)} \right) \frac{\phi_{i+1} - 2\phi_i + \phi_{i-1}}{h^2} = 0 \tag{29}$$

By comparing the following exact equation for (28)

$$u \frac{\phi_{i+1} - \phi_{i-1}}{2h} - \frac{uh}{2} \coth\left(\frac{uh}{2\mu} \right) \frac{\phi_{i+1} - 2\phi_i + \phi_{i-1}}{h^2} = 0 \tag{30}$$

we can derive the upwinding coefficient τ, which is expressed in terms of $\gamma (\equiv \frac{uh}{2\mu})$, as follows

$$\tau = \frac{w(h)}{u w'(h)} \frac{\gamma \coth(\gamma) - 1}{\gamma} \tag{31}$$

By expanding the terms $\phi_{i+1,j+1}, \phi_{i+1,j-1}, \phi_{i-1,j+1}, \phi_{i-1,j-1}, \phi_{i-1,j}, \phi_{i+1,j}, \phi_{i,j+1}$, and $\phi_{i,j-1}$ in a Taylor series about $\phi_{i,j}$ and then substituting them into the discrete equation for (4), one can easily derive the following modified equation

$$u \frac{\partial \phi}{\partial x} + v \frac{\partial \phi}{\partial y} - \mu \left(\frac{\partial^2 \phi}{\partial x^2} + \frac{\partial^2 \phi}{\partial y^2} \right) = a \frac{\partial^2 \phi}{\partial x^2} + b \frac{\partial^2 \phi}{\partial x \partial y} + c \frac{\partial^2 \phi}{\partial y^2} + \cdots \tag{32}$$

Let $m = \frac{4(-512\sqrt{2}+745)}{1125(32\sqrt{2}-47)} \frac{\gamma \coth(\gamma) - 1}{\gamma} h^2$, the coefficients of the leading error terms shown above can be expressed as

$$a = \frac{9u^2 + v^2}{\sqrt{u^2 + v^2}} m \tag{33}$$

$$b = \frac{4uv}{\sqrt{u^2 + v^2}} m \tag{34}$$

$$c = \frac{u^2 + 9v^2}{\sqrt{u^2 + v^2}} m \tag{35}$$

Through the above modified equation analysis, we know from the value of m and Eqs. (32)–(35) that the enhanced stability along the streamline direction is at the cost of deteriorating the solution
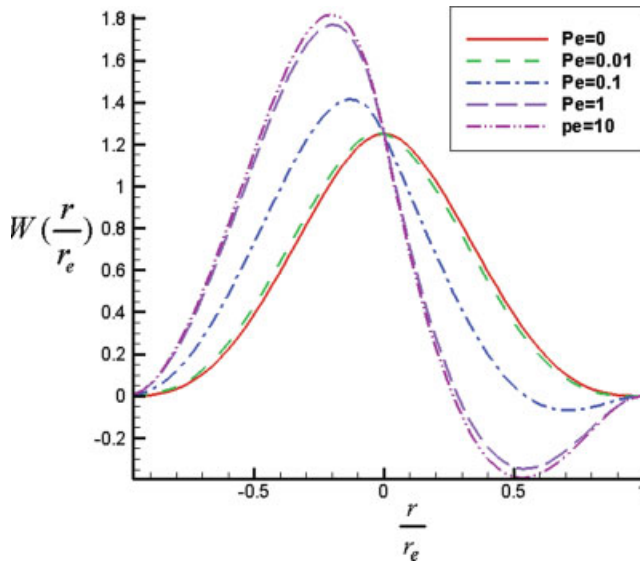
FIG. 2.   The developed upwinding kernel function, given in Eqs. (26, 27, 31), is plotted at $u = 1$, $v = 1$ for the cases investigated at different Peclet numbers 0, 0.01, 0.1, 1, and 10. [Color figure can be viewed in the online issue, which is available at wileyonlinelibrary.com.]

accuracy by two orders of magnitude, in comparison with the fourth-order accurate center-type interaction model.

For making a clear comparison of the developed center and upwinding kernel functions, the upwind-type kernel function recommended for use in the high Peclet number flow simulation will be also plotted. In Fig. 2, $W(r)$ in (26) is plotted for the case investigated, for example, at $u = v = 1$ and different values of μ that render the respective Peclet numbers with the values of $Pe = 0, 0.01, 0.1, 1$, and 10. Note that $\int_{-r_e}^{r_e} W(r)d\Omega$ is, as before, equal to one for the upwinding kernel derived in (26).

V. NUMERICAL RESULTS

Several problems regarding the transport of ϕ, governed by Eq. (4), will be solved to analytically verify the proposed particle method. We first solve the Laplace equation in a unit square, which has been uniformly discretized at different mesh sizes $\Delta x = \Delta y = 0.25, 0.1666, 0.125, 0.1$. Calculation of this elliptic equation, subject to the analytic boundary condition $\phi = Tan^{-1}[\frac{x-2}{y-2}]$, will be carried out. The predicted L_2-error norms are tabulated in Table I, from which we can see

TABLE I.   The predicted L_2-error norms and their corresponding rates of convergence in different meshes when solving the Laplace equation based on the center-type kernel function.

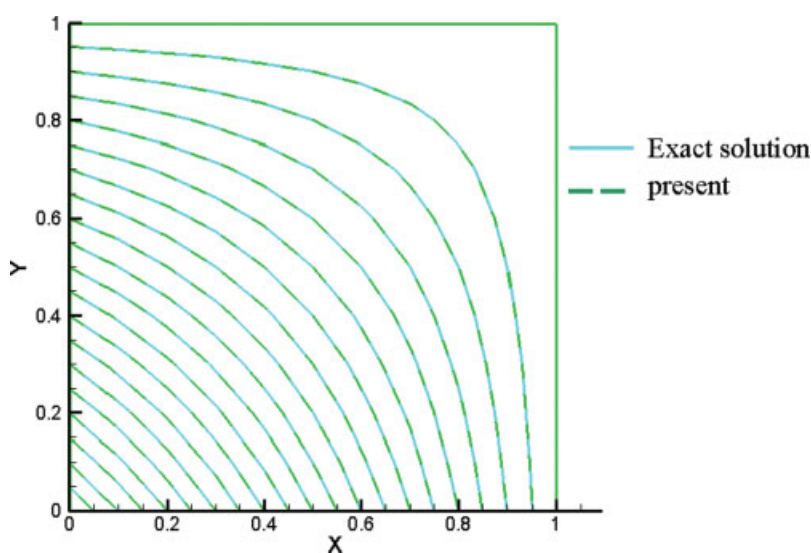| Meshes	L_2-error norms	Rates of convergence
5×5	1.811×10^{-8}	
7×7	1.571×10^{-9}	7.26584
9×9	2.681×10^{-10}	7.03544
11×11	6.674×10^{-11}	6.92954

FIG. 3.   Comparison of the exact solution with the predicted solution at $Pe = 1 \times 10^{-3}$ for the problem with the exact solution given in Eq. (36). The predicted solutions are computed by the proposed center-type kernel function. [Color figure can be viewed in the online issue, which is available at wileyonlinelibrary.com.]

that the predicted rate of convergence is surprisingly higher than its theoretical value of fourth due probably to the machine error.

The next problem under current investigation has the following smoothly distributed analytic solution, defined in $0 \leq x, y \leq 1$, for Eq. (4).

$$\phi = \frac{(1 - e^{(x-1)u/\mu})(1 - e^{(y-1)v/\mu})}{(1 - e^{-u/\mu})(1 - e^{-v/\mu})} \tag{36}$$

Calculation will be carried out first at the fixed Peclet number $Pe(\equiv uh/\mu) = 0.00001$, where h denotes the grid size, to justify the developed center-type kernel function. The solutions predicted at $\mu = 10,000$ using the center-type kernel function given in (22) are seen to agree excellently with the exact solution plotted in Fig. 3. The proposed kernel function is therefore confirmed to be applicable to solve the problem with a Peclet number smaller than 2. Calculation is followed by solving Eq. (4) in different meshes. As Table II shows, the predicted solutions agree quite well with the theoretical solution for the case investigated at $\mu = 10,000$ using the center-type kernel function.

TABLE II.   The predicted L_2-error norms at different meshes when solving the convection-diffusion equation at $\mu = 10,000$ based on the center-type kernel function.

Meshes	L_2-error norms
10×10	3.890×10^{-14}
20×20	9.455×10^{-15}
30×30	5.511×10^{-15}
40×40	5.350×10^{-15}
50×50	2.406×10^{-15}

TABLE III.   The predicted L_2-error norms and their corresponding rates of convergence using the upwinding kernel function to solve the Eq. (4) at $\mu = 0.01$.

Meshes	L_2-error norms	Rates of convergence
60×60	1.612×10^{-2}	
70×70	1.188×10^{-2}	1.97991
80×80	9.088×10^{-3}	2.00628
90×90	7.163×10^{-3}	2.02089
100×100	5.788×10^{-3}	2.02298

The upwinding-type kernel function is then applied to solve the same problem but with a much smaller value of μ, say at $\mu = 0.01$, for making the equation to be convection dominated. The rates of convergence, tabulated in Table III, are computed from the L_2-error norms of the solutions calculated from the upwinding-type kernel function. Under our expectation, the predicted rates of convergence are approximately equal to 2 owing to the numerical damping terms shown in (32)–(35).

Verification of the proposed particle model is followed by solving the following two analytic problems under higher Peclet number flow conditions. One problem has an interior layer and the other problem has the interior as well as the boundary layers.

A. Convection Dominated Scalar Transport Problems

We will then apply the developed upwinding kernel function to simulate the high-Peclet number flow problems. Three problems with different solution natures will be considered below.

A.1 Convection-Diffusion Problem of Smith and Hutton

The problem of Smith and Hutton [18] will be investigated in a divergence-free flowfield defined by $u = 2y(1 - x^2)$ and $v = -2x(1 - y^2)$, which are shown in Eq. (4). Along the inlet schematic in Fig. 4, the boundary value of ϕ along $-1 \leq x \leq 0$, $y = 0$ is prescribed by $\phi = 1 + \tanh[10(2x + 1)]$. Along the lines $x = -1$, $y = 1$, and $x = 1$, ϕ is prescribed to have
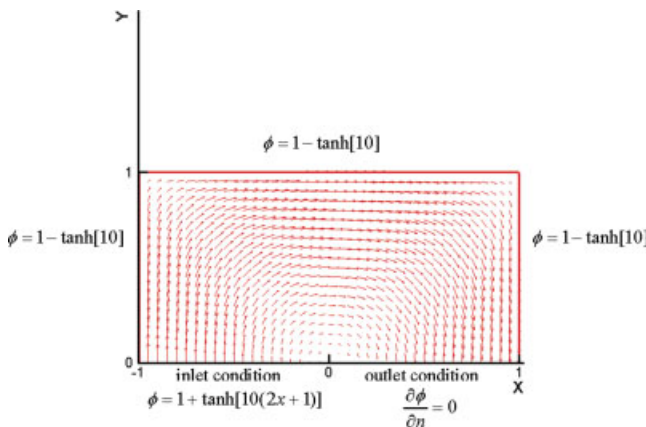

FIG. 4.   Schematic of the boundary conditions and the initially prescribed velocity vectors for the Smith and Hutton problem. [Color figure can be viewed in the online issue, which is available at wileyonlinelibrary.com.]
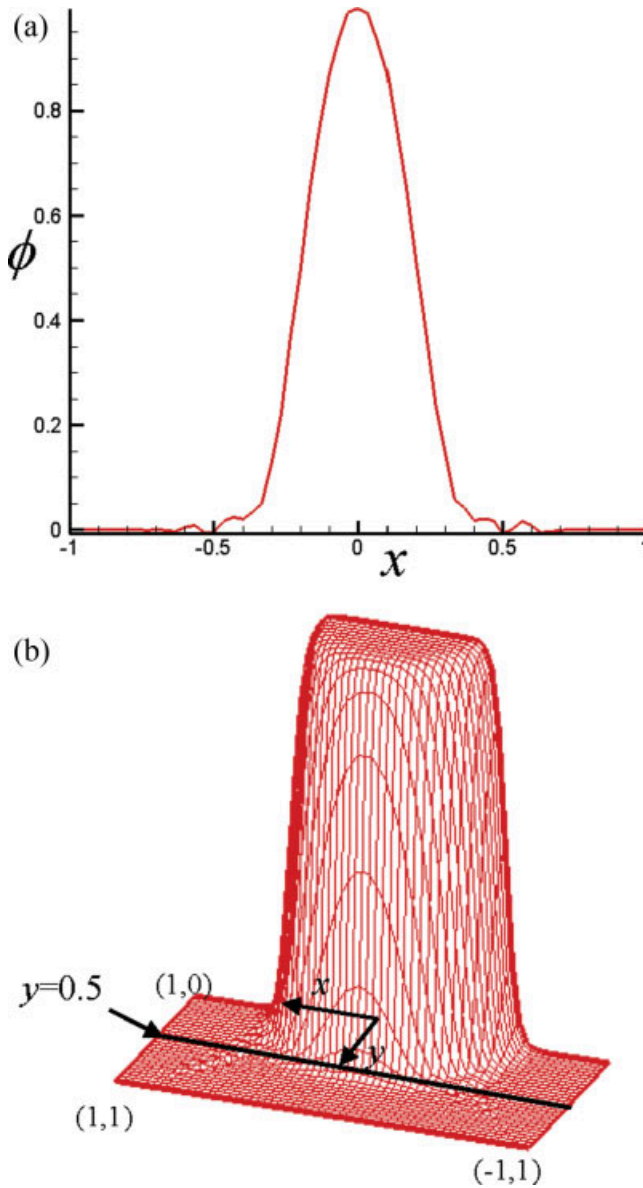
FIG. 5.   Illustration of the predicted oscillatory solution using the center-type kernel function to solve the Smith and Hutton problem at $\mu = 0.00001$. (a) The plot of Φ along the line $(x, y = 0.5)$. (b) Three dimensional plot of the predicted value of Φ. [Color figure can be viewed in the online issue, which is available at wileyonlinelibrary.com.]

the magnitude $1 - \tanh(10)$, while along the outlet $(0 \leq x \leq 1, y = 0)$ a zero gradient condition is specified.

For the case investigated at $\mu = 0.0001$, the results will be calculated at $\Delta x = \Delta y = \frac{1}{40}$. As Fig. 5 shows, the predicted oscillatory solution is the result of using the centered scheme that suffers the problem of instability for the convection-dominated problem [19]. To suppress numerical
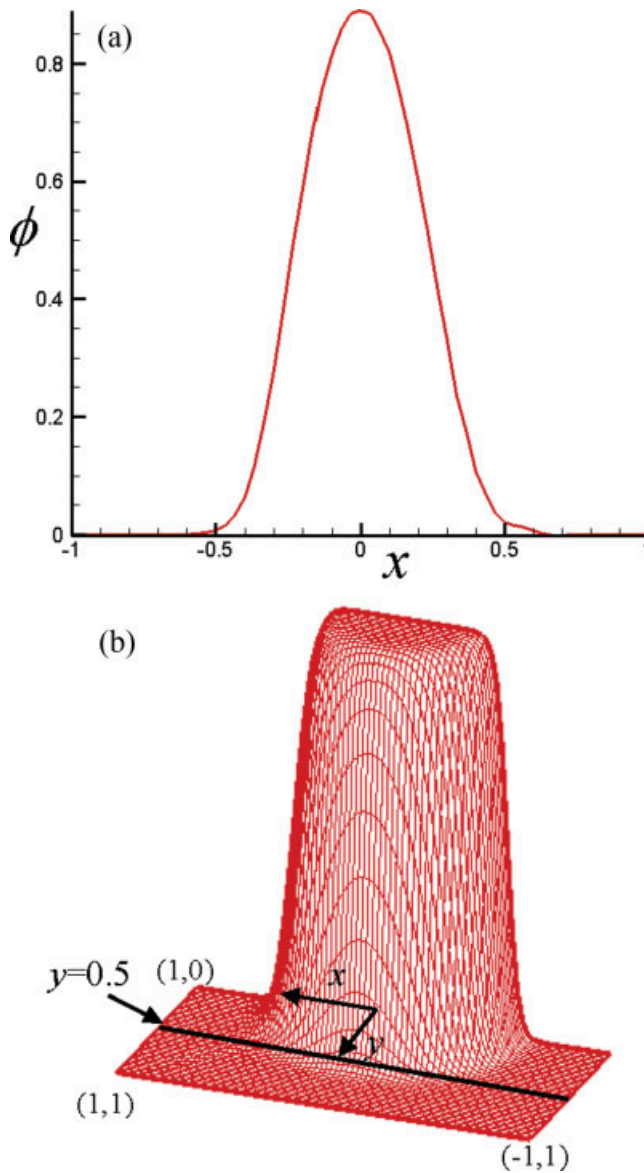
FIG. 6.   The plot of the predicted nonoscillatory solution using the upwinding kernel function to solve the Smith and Hutton problem at $\mu = 0.0001$. (a) The plot of Φ along the line $(x, y = 0.5)$. (b) Three dimensional plot of the predicted value of Φ. [Color figure can be viewed in the online issue, which is available at wileyonlinelibrary.com.]

instability, one can damp out these oscillations by the implicitly added damping term introduced into the upwinding-type particle method. It can be seen from Fig. 6 that the predicted solution is essentially non-oscillatory. The efficacy of applying the proposed upwind-type particle model to simulate the high Peclet number flow is therefore demonstrated using the problem involving an interior sharp layer.
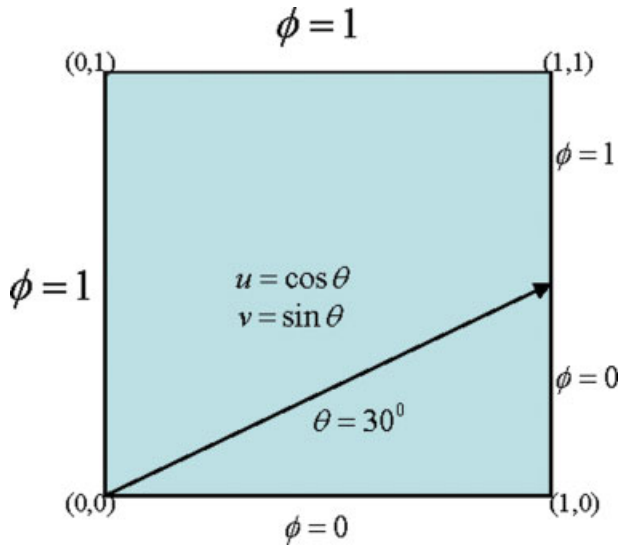
FIG. 7.   Schematic of the skew convection-diffusion problem. [Color figure can be viewed in the online issue, which is available at wileyonlinelibrary.com.]

A.2 Skew Convection-Diffusion Problem.   In Fig. 7, a square cavity of unit length is divided into two subdomains by the straight line passing through $(0, 0)$ with the slope of $\tan^{-1}(v/u)$, where u and v are shown in Eq. (4). We consider in this study the unit velocity vector (u, v), which is parallel to the dividing line, in the 21×21 (for $\mu = 0.001$ and $\mu = 0.00001$) uniformly discretized mesh system. Subject to the boundary conditions for ϕ, one can clearly see from the computed solution in Fig. 8 that a shear layer exists in the vicinity of the dividing line. No oscillatory solution is found in regions near and apart from the dividing line for the cases investigated at $\mu = 0.001$ and $\mu = 0.00001$.

A.3 Gartland Problem.   The problem involving a sharply varying solution near the boundary along the downstream edge at $x = 1$ and two shear layers along the top and bottom edges at $y = 0$ and $y = 1$ will be also investigated. This boundary/shear layer problem with $\mu = 0.01$ will be solved in a square of unit length at $(u, v) = (1, 0)$.

By specifying the boundary condition according to the following exact solution [20]

$$\phi = e^{\frac{x}{2\mu}} \sin \pi y \frac{2e^{\frac{-1}{2\mu}} \sinh \lambda x + \sinh \lambda (1 - x)}{\sinh \lambda} \tag{37}$$

our calculation will be performed at $u = 1$ and $\lambda = \pi^2 + \frac{1}{4\mu^2}$. As Fig. 9 shows, near the boundaries at $x = 1$, $y = 0$, and $y = 1$ one can clearly find the predicted non-oscillatory high gradient solution profile. For completeness, we solve the same problem in different meshes with an aim to calculate the corresponding rates of convergence, which are approximately equal to the theoretical rate, tabulated in Table IV.

For the sake of comparison of our computed and the other numerical solutions, we also carry out the calculation for the case with $\mu = 0.01$ in eight meshes 8^2, 16^2, 32^2, 64^2, 70^2, 80^2, 90^2, and 100^2. All the predicted maximum errors, tabulated in Table V, are seen to be smaller than
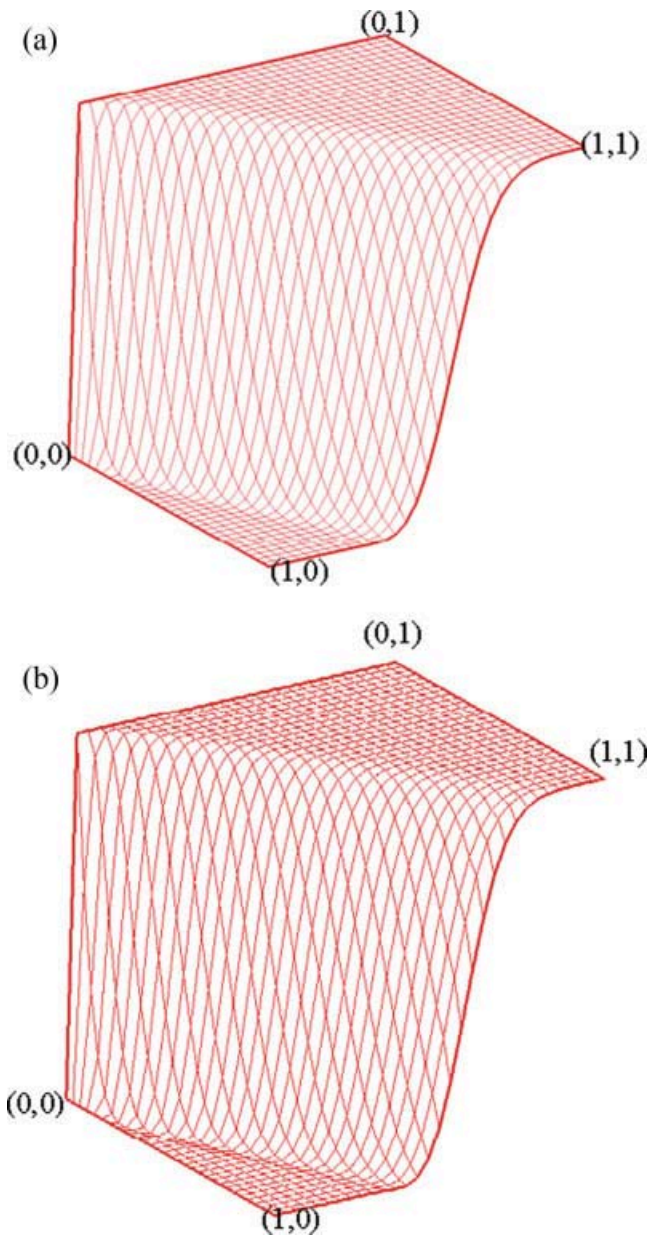
FIG. 8.   The prescribed nonoscillatory solution profiles for the skew advection-diffusion problem investigated at two values of μ. (a) $\mu = 0.001$. (b) $\mu = 0.00001$. [Color figure can be viewed in the online issue, which is available at wileyonlinelibrary.com.]

those predicted by the second-order accurate central scheme CDS but are larger than those by the DWMA scheme of Gartland [20] and the SCHOS scheme of Gupta et al. [21]. The rates of convergence based on the computed results in Table V are equal to the theoretical rate as well.
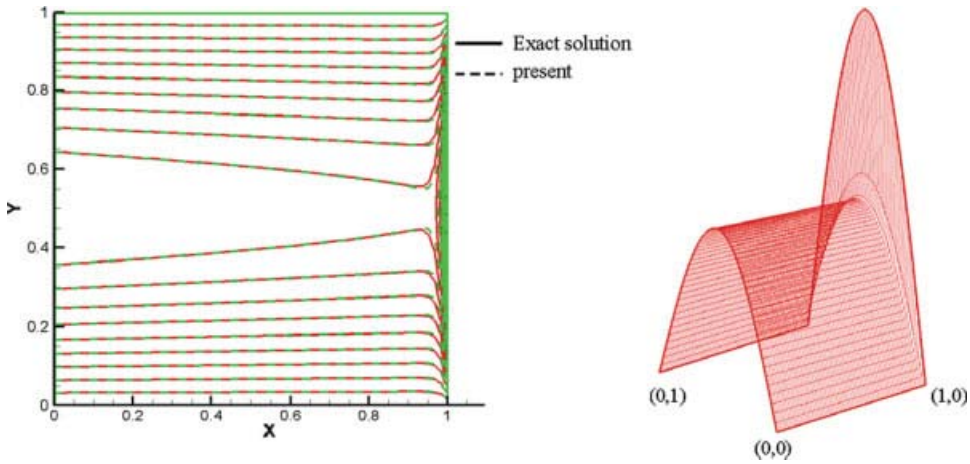
FIG. 9. Comparison of the exact and predicted solutions for the test problem given in Section V.A.3. (a) Contour plot of Φ. (b) The predicted sharp layer near $x = 1$ and the two boundary layers $y = 0$ and $y = 1$. [Color figure can be viewed in the online issue, which is available at wileyonlinelibrary.com.]

TABLE IV. The predicted L_2-error norms and the corresponding rates of convergence in five meshes 60×60, 70×70, 80×80, 90×90, and 100×100 using the upwinding particle interaction model to solve the test problem given in section V.A.3.

Meshes	L_2-error norms	Rates of convergence
60×60	7.985×10^{-3}	
70×70	5.901×10^{-3}	1.96200
80×80	4.534×10^{-3}	1.97345
90×90	3.592×10^{-3}	1.97733
100×100	2.918×10^{-3}	1.97238

TABLE V. The predicted maximum errors and their corresponding rates of convergence ($O(h^{\text{rate of convergence}})$) in eight meshes 8^2, 16^2, 32^2, 64^2, 70^2, 80^2, 90^2, and 100^2 using the upwinding particle interaction model, to solve the Gartland test problem [20].

Meshes	DWMA [18] maximum error	CDS [19] maximum error	SCHOS [19] maximum error	Center-type maximum error (current)	Upwind-type maximum error (current)	Upwind-type L_2-error norm (current)
8×8	3.685×10^{-2}	9.060×10^{-1}	4.248×10^{-1}	9.143×10^{-1}	2.404×10^{-1}	7.799×10^{-2}
16×16	5.812×10^{-2}	5.618×10^{-1}	1.670×10^{-1}	5.633×10^{-1}	2.890×10^{-1}	5.601×10^{-2}
	$O(h^{-0.65737})$	$O(h^{0.689454})$	$O(h^{1.34694})$	$O(h^{0.698764})$	$O(h^{-0.265633})$	$O(h^{0.477605})$
32×32	4.993×10^{-2}	2.873×10^{-1}	3.365×10^{-2}	2.876×10^{-1}	1.916×10^{-1}	2.488×10^{-2}
	$O(h^{0.219128})$	$O(h^{0.967499})$	$O(h^{2.31117})$	$O(h^{0.969840})$	$O(h^{0.592972})$	$O(h^{1.17070})$
64×64	2.106×10^{-2}	9.493×10^{-2}	3.151×10^{-3}	9.490×10^{-2}	7.301×10^{-2}	7.038×10^{-3}
	$O(h^{1.2454})$	$O(h^{1.59762})$	$O(h^{3.41672})$	$O(h^{1.59958})$	$O(h^{1.39193})$	$O(h^{1.82175})$
70×70	N.A.	N.A.	N.A.	7.980×10^{-2}	6.235×10^{-2}	5.901×10^{-3}
				$O(h^{1.93389})$	$O(h^{1.76129})$	$O(h^{1.96628})$
80×80	N.A.	N.A.	N.A.	6.095×10^{-2}	4.870×10^{-2}	4.534×10^{-3}
				$O(h^{2.01802})$	$O(h^{1.85039})$	$O(h^{1.97345})$
90×90	N.A.	N.A.	N.A.	4.755×10^{-2}	3.873×10^{-2}	3.592×10^{-3}
				$O(h^{2.10788})$	$O(h^{1.94480})$	$O(h^{1.97733})$
100×100	N.A.	N.A.	N.A.	3.779×10^{-2}	3.128×10^{-2}	2.918×10^{-3}
				$O(h^{2.18049})$	$O(h^{2.02766})$	$O(h^{1.97238})$

TABLE VI. The predicted L_2-error norms and their corresponding rates of convergence for the Navier-Stokes equations.

Meshes	L_2-error norms of u	Rates of convergence
11×11	9.307×10^{-5}	
21×21	2.161×10^{-5}	2.10662
31×31	1.012×10^{-5}	1.87104
41×41	5.865×10^{-6}	1.89623

B. Incompressible Navier-Stokes Problems

With the success of applying the center and upwinding kernel functions to simulate the low and high Peclet number problems, we will then apply the developed kernel function to predict the incompressible Navier-Stokes equations.

To begin with, we consider the problem that is amenable to the analytic solutions. For this problem, a square domain of unit length is discretized into uniform rectangular mesh. The exact pressure for Eqs. (1)–(3) takes the following form

$$p = \frac{-2}{(1 + x)^2 + (1 + y)^2} \tag{38}$$

on condition that the boundary velocities are specified analytically as follows:

$$u = \frac{-2(1 + y)}{(1 + x)^2 + (1 + y)^2} \tag{39}$$

$$v = \frac{2(1 + x)}{(1 + x)^2 + (1 + y)^2} \tag{40}$$

The predicted L_2-error norms and their corresponding spatial rates of convergence computed at different meshes are shown in Table VI.

We then solve a more stringent test problem, which is also amenable to the analytic solution given by

$$u = 1 - e^{\lambda x} \cos(2\pi y) \tag{41}$$

$$v = \frac{\lambda}{2\pi} e^{\lambda x} \sin(2\pi y) \tag{42}$$

$$p = \frac{1}{2}(1 - e^{2\lambda x}) \tag{43}$$

In this study, the value of λ is chosen to be $\lambda = \frac{Re}{2} - \sqrt{\frac{Re^2}{4} + 4\pi^2}$. For the calculation performed at $Re = 100$, the predicted L_2-error norms in four meshes and their corresponding rates of convergence are tabulated in Table VII.

The third example is known to be the lid-driven cavity problem which is well documented in the literature. This problem has received a great deal of attention mainly because of its geometrical simplicity and physical complexity. The boundary velocities u and v are zero everywhere except along the top surface where $u = 1$ and $v = 0$. Computations are performed at the Reynolds numbers 100 and 1000 in the respective regular meshes of 41×41 and 151×151.

For the sake of comparison, the results for the calculations computed at $Re = 100$ and 1000 are plotted along the mid-sectional horizontal and vertical lines in Figs. 10 and 11, respectively. The present results compare well with the finite difference solutions of Ghia et al. [22].

TABLE VII.   The L_2-error norms and their corresponding rates of convergence predicted in different meshes.

Meshes	L_2-error norms of u	Rates of convergence
11×11	1.082×10^{-3}	
21×21	6.948×10^{-5}	3.96096
31×31	1.603×10^{-5}	3.61702
41×41	6.756×10^{-6}	3.00342

We also consider the two-dimensional stationary incompressible channel flow around a circular cylinder [23]. In Fig. 12, D denotes the cylinder diameter, and H is the channel height. The parabolic profile schematic in Fig. 12 is prescribed at the channel inlet and outlet, and no-slip conditions are imposed at the solid boundaries. In this flow calculation, Reynolds number is $Re = 20$, which is calculated on the basis of choosing the dynamic viscosity $\mu = 0.001 \, \mathrm{kg \, m^{-1} \, s^{-1}}$, density of the flow $\rho = 1 \, \mathrm{kg \, m^{-3}}$, mean inflow velocity $U = 0.2 \, \mathrm{m \, s^{-1}}$, and the diameter of the cylinder $D = 0.1 \, \mathrm{m}$. The computed pressure and streamline contours are shown in Fig. 13.

The benchmark parameters chosen for the sake of comparison are the drag coefficient C_d of the cylinder and the pressure difference between the front and the rear of the cylinder. The computed drag coefficient and pressure difference compare well with the reference values given in [23] ($C_{d,ref} = 5.57953523384$ and $\Delta p_{ref} = 0.11752016697$), and the details of comparison are tabulated in Table VIII.

The fifth problem under current investigation considers the flow over a square. The blockage ratio $\beta(=D/H)$ is specified as $1/8$ (D: the size of square cylinder; H: the height of the channel). For the Reynolds number defined by $Re = \frac{\rho u_{max} D}{\mu}$, where u_{max} is the maximum inlet flow velocity
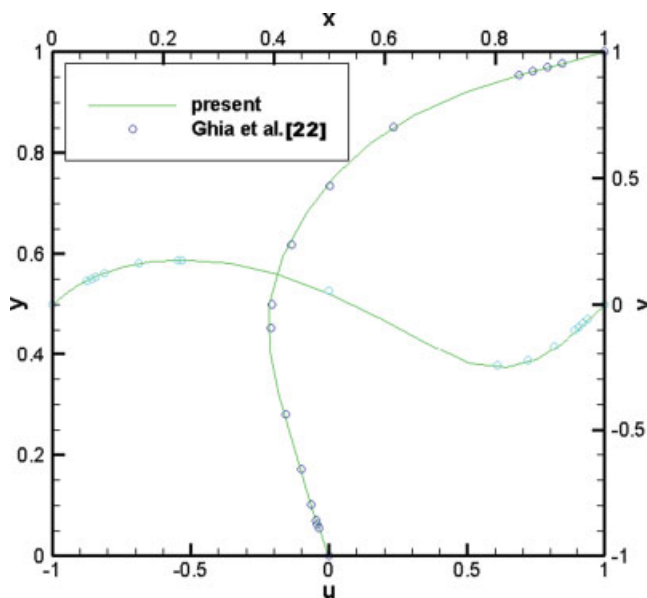

FIG. 10.   Comparison of the predicted and referenced velocity profiles of u at $x = 0.5$ and v at $y = 0.5$ for the case investigated at $Re = 100$. [Color figure can be viewed in the online issue, which is available at wileyonlinelibrary.com.]
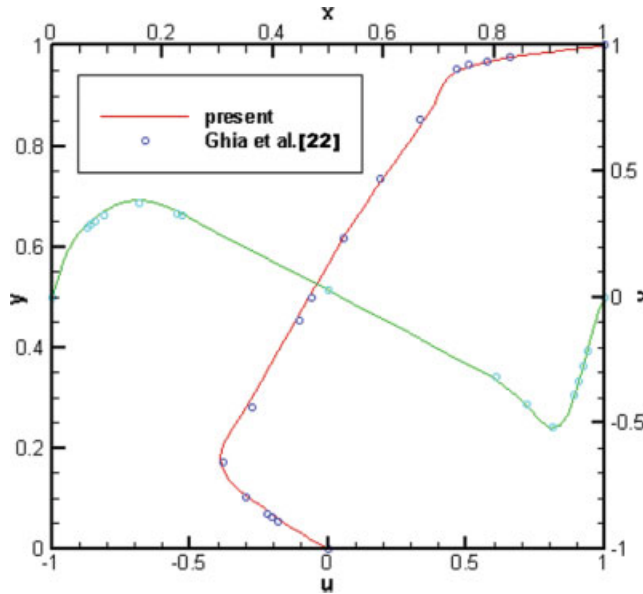
FIG. 11.   Comparison of the predicted and referenced velocity profiles of u at $x = 0.5$ and v at $y = 0.5$ for the case investigated at $Re = 1000$. [Color figure can be viewed in the online issue, which is available at wileyonlinelibrary.com.]

and μ is the dynamic viscosity, we simulate the flow at $Re = 30$. The pressure and streamline contours are shown in Fig. 14. Figure 15 plots the computed recirculation lengths L_r against the Reynolds number for a square cylinder inside a channel ($L_r = -0.065 + 0.0554\ Re$, for $5 < Re < 60$ [24]). As can be seen from this figure, reliable and accurate results have been obtained by the proposed particle method.

VI. CONCLUDING REMARKS

As a first step toward our future simulation of unsteady interfacial flow problem by the moving particle method, we develop a kernel function within the stationary particle framework so as to facilitate the theoretical derivation. The idea of developing the proposed particle interaction
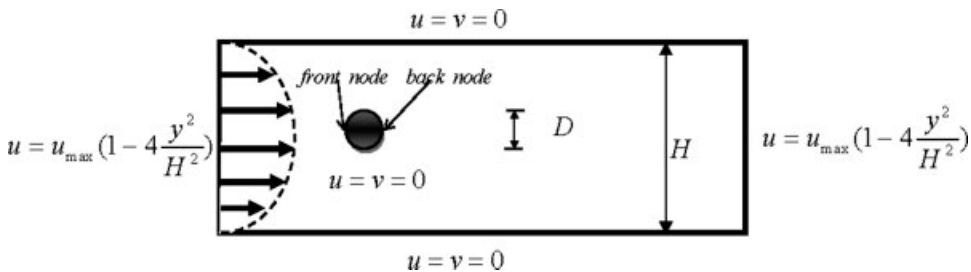

FIG. 12.   Schematic of the channel flow around a circular cylinder.

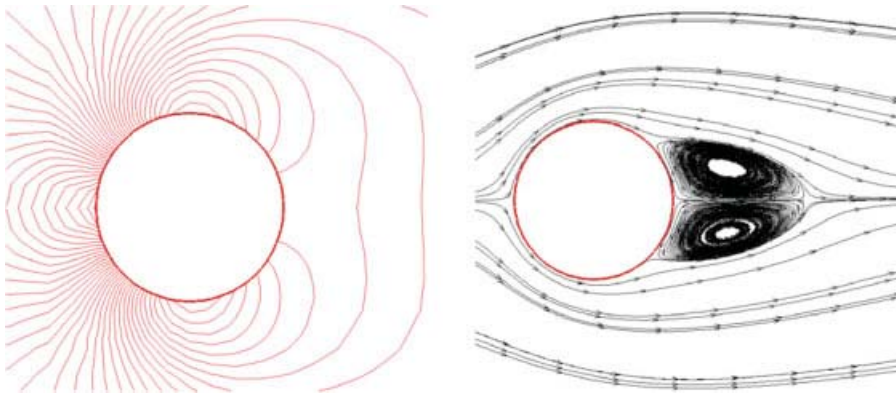*Numerical Methods for Partial Differential Equations* DOI 10.1002/num

FIG. 13.   The computed pressure and streamline contours at $Re = 20$. [Color figure can be viewed in the online issue, which is available at wileyonlinelibrary.com.]

TABLE VIII.   Comparison of the values of C_d and Δp obtained in different meshes at $Re = 20$ with those in [23] for the flow around a circular cylinder.

Meshes	C_d	$\Delta p = p_f - p_b$
3528 nodes	5.25778877	0.11912604625
12,368 nodes	5.37865958	0.11880092234
16,368 nodes	5.46402895	0.11837051836
20,000,00 nodes Volker [23]	5.57953523384	0.11752016697

model is to formulate the kernel function, which accommodates the property embedded in the smoothed Dirac delta function, for the pure diffusion (or Laplace) equation. The center-type kernel function, which is constrained by $\int_{\frac{r}{re}=-1}^{\frac{r}{re}=1} w(r)dr = 1$ in the users' chosen particle interaction region, is by adding a flow-direction dependent term to the center-type kernel function to enhance
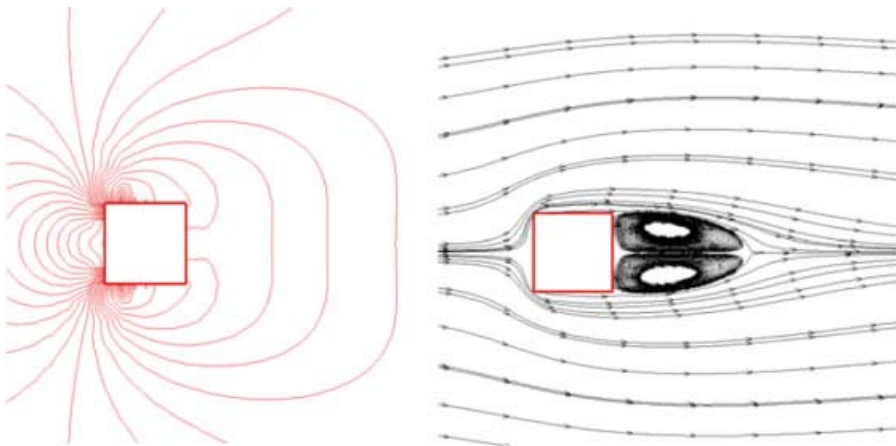

FIG. 14.   The computed pressure and streamline contours at $Re = 30$. [Color figure can be viewed in the online issue, which is available at wileyonlinelibrary.com.]
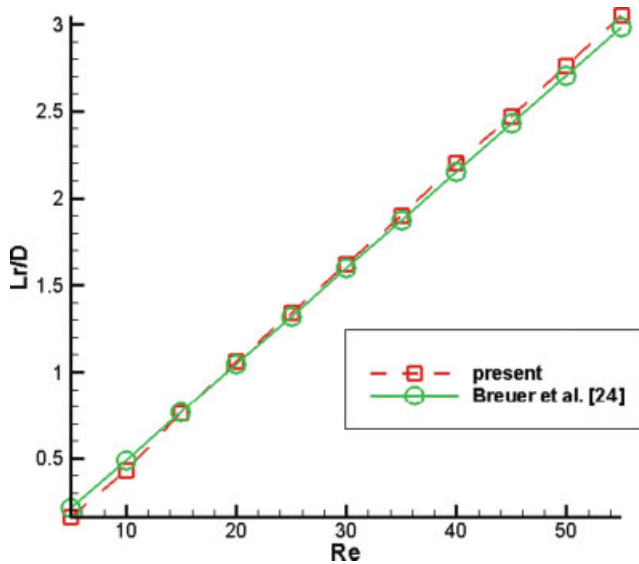
Numerical Methods for Partial Differential Equations DOI 10.1002/num

FIG. 15.   Comparison of the computed recirculation lengths L_r against the Reynolds number based on the results obtained in a mesh with 5000 nodal points. [Color figure can be viewed in the online issue, which is available at wileyonlinelibrary.com.]

numerical stability by means of the introduced streamline diffusion in case when the convection term becomes increasingly larger than the diffusion term. For the purpose of getting this stability enhancement, we implicitly add the diffusion term mainly along the flow direction so that the upstream particles can be more weighted. To justify the centered and upwinding kernel functions developed for simulating the respective low and high Peclet number flows, we investigate several well-known benchmark problems for the validation sake. These predicted results clearly show that the second-order accurate upwinding particle interaction model can capture well the interior as well as the boundary layers without showing numerical oscillations in the region of sharp gradients.

APPENDIX A: DERIVATION OF THE DISCRETE EQUATION (18)

Derivation is started from the Eq. (9), which is

$$\langle \nabla^2 \phi \rangle|_i = \frac{2d}{\lambda n^0} \sum_{j \neq i} (\phi_j - \phi_i)^w (|\underline{r}_j - \underline{r}_i|) \tag{9}$$

In the domain of uniform meshes with the grid size h, $n^0 (\equiv \sum_{j \neq i} w(|\underline{r}_j - \underline{r}_i|))$ is equal to

$$n^0 = \sum_{i \neq j} w(|r_j^0 - r_i^0|) = 4(w(h) + w(\sqrt{2}h)) \tag{A1}$$

By virtue of Eq. (10), we can get

$$\lambda = \frac{[w(h) + 2w(\sqrt{2}h)]h^2}{[w(h) + w(\sqrt{2}h)]} \tag{A2}$$

By substituting the values n^0 and λ shown, respectively, in (A1) and (A2), we can derive the second-order accurate modified equation for the two-dimensional Equation (9)

$$\frac{1}{[w(h) + 2w(\sqrt{2}h)]h^2}\{(\phi_{i+1,j} + \phi_{i-1,j} + \phi_{i,j+1} + \phi_{i,j-1} - 4\phi_i)w(h)$$
$$+ (\phi_{i+1,j+1} + \phi_{i-1,j+1} + \phi_{i+1,j-1} + \phi_{i-1,j-1} - 4\phi_i)w(\sqrt{2}h)\} = 0 \quad (18)$$

APPENDIX B: DERIVATION OF THE STREAMLINE DIFFUSION TERM ϕ_{SS}

Given a flow with a velocity vector (u, v), its local tangential direction is given by $s = \tan^{-1}(\frac{v}{u})$. By substituting $\frac{\partial s}{\partial x} = \frac{\sqrt{u^2+v^2}}{u}$ and $\frac{\partial s}{\partial y} = \frac{\sqrt{u^2+v^2}}{v}$ into the following equation

$$\frac{\partial \phi}{\partial s} = \frac{\partial \phi}{\partial x}\frac{\partial x}{\partial s} + \frac{\partial \phi}{\partial y}\frac{\partial y}{\partial s} = \frac{\partial \phi}{\partial x}\frac{1}{\frac{\partial s}{\partial x}} + \frac{\partial \phi}{\partial y}\frac{1}{\frac{\partial s}{\partial y}} \tag{B1}$$

we can get

$$\frac{\partial \phi}{\partial s} = \frac{u}{\sqrt{u^2 + v^2}}\frac{\partial \phi}{\partial x} + \frac{v}{\sqrt{u^2 + v^2}}\frac{\partial \phi}{\partial y} \tag{B2}$$

By applying the differential operator $\partial/\partial s$ on Eq. (B2), we can get Eq. (25) for ϕ_{ss} as follows

$$\frac{\partial^2 \phi}{\partial s^2} = \frac{\partial}{\partial s}\left(\frac{\partial \phi}{\partial s}\right) = \frac{\partial}{\partial s}\left(\frac{u}{\sqrt{u^2 + v^2}}\frac{\partial \phi}{\partial x} + \frac{v}{\sqrt{u^2 + v^2}}\frac{\partial \phi}{\partial y}\right)$$
$$= \frac{\partial}{\partial x}\left(\frac{u}{\sqrt{u^2 + v^2}}\frac{\partial \phi}{\partial x} + \frac{v}{\sqrt{u^2 + v^2}}\frac{\partial \phi}{\partial y}\right)\frac{\partial x}{\partial s} + \frac{\partial}{\partial y}\left(\frac{u}{\sqrt{u^2 + v^2}}\frac{\partial \phi}{\partial x} + \frac{v}{\sqrt{u^2 + v^2}}\frac{\partial \phi}{\partial y}\right)\frac{\partial y}{\partial s}$$
$$= \frac{u^2}{u^2 + v^2}\frac{\partial^2 \phi}{\partial x^2} + \frac{2uv}{u^2 + v^2}\frac{\partial^2 \phi}{\partial x \partial y} + \frac{u^2}{u^2 + v^2}\frac{\partial^2 \phi}{\partial y^2}$$

References

1. C. W. Hirt, A. A. Amsden, and J. L. Cook, An arbitrary Lagrangian-Eulerian computing method for all flow speeds, J Comput Phys 14 (1974), 227–253.

2. F. H. Harlow and J. E. Welch, Numerical calculation of time-dependent viscous incompressible flow of fluid with a free surface, Phys Fluids 8 (1965), 2182–2189.

3. C. W. Hirt and B. D. Nicholls, Volume of fluid (VOF) method for dynamics of free boundaries, J Comput Phys 39 (1981), 201–221.

4. S. Osher and R. P. Fedkiw, Level set methods: An overview and some recent results, J Comput Phys 169 (2001), 463–502.

5. F. H. Harlow and A. Machine, Calculation method for hydrodynamic problems, 1955.

6. L. B. Lucy, A numerical approach to the testing of the fission hypothesis, Astro J 82 (1977), 1013–1024.

7. R. A. Gingold and J. J. Monaghan, Smoothed particle hydrodynamics: theory and application to nonspherical stars, Astrophys J 181 (1977), 275–389.

8. J. J. Monaghan, Simulating free surface flows with SPH, J Comput Phys 110 (1994), 399–406.

9. S. Koshizuka, H. Tamako, and Y. Oka, A particle method for incompressible viscous flow with fluid fragmentation, Comput Fluid Dyn J 4 (1995), 29–46.

10. J. Onderik and R. Durikovic, Efficient neighbor search for particle-based fluids, J Appl Math Stat Inform 4 (2008), 29–43.

11. B. Ataie-Ashtiani and L. Farhadi, A stable moving-particle semi-implicit method for free surface flows, Fluid Dyn Res 38 (2006), 241–256.

12. S. Zhang, K. Morita, K. Fukuda, and N. Shirakawa, An improved MPS method for numerical simulations of convective heat transfer problems, Int J Numer Meth Fluids 51 (2006), 31–47.

13. T. Belytschko, Y. Krongaux, D. Organ, M. Fleming, and P. Krys, Meshless methods: an overview and recent developments, Comput Method Appl Mech Eng 139 (1996), 3–47.

14. S. Koshizuka and Y. Oka, Moving-particle semi-implicit method for fragmentation of incompressible fluids, Nucl Sci Eng 123 (1996), 421–434.

15. S. Kohizuka, A. Nobe, and Y. Oka, Numerical analysis of breaking waves using the moving particle semi-implicit method, Int J Numer Meth Fluid 26 (1998), 751–769.

16. A. Brooks and T. J. R. Hughes, Streamline upwind/Petrov Galerkin formulations for convection dominated flows with particular emphasis on the incompressible Navier-Stokes equations, Comput Meth Appl Mech Eng 32 (1982), 199–259.

17. T. W. H. Sheu, S. F. Tsai, and M. M. T. Wang, A Petrov Galerkin formulation for incompressible flows at high Reynolds numbers, J Comput Fluid Dyn 5 (1995), 213–230.

18. R. M. Smith and A. G. Hutton, The numerical treatment of convection– a performance comparison of current methods, Numer Heat Transfer 5 (1982), 439–461.

19. J. Zhang and J. J. Zhao, Truncation error and oscillation property of the combined compact difference scheme, Appl Math Comput 161 (2005), 241–251.

20. E. C. Gartland, Discrete weighted mean approximation of a model convection-diffusion equation, SIAM J Sci Statist Comput 3 (1982), 460–472.

21. M. M. Gupta, R. P. Manohar, and J. W. Stephenson, High-order difference schemes for two-dimensional elliptic equations, Numer Meth Partial Differ Equat 1 (1985), 71–80.

22. U. Ghia, K. N. Ghia, and C. T. Shin, High-re solutions for incompressible flow using the Navier-Stokes equations and a multigrid method, J Comput Phys 48 (1982), 387–411.

23. V. John and G. Matthies, Higher-order finite element discretizations in a benchmark problem for incompressible flows, Int J Numer Meth Fluid 37 (2001), 885–903.

24. M. Breuer, J. Bernsdorf, T. Zeiser, and F. Durst, Accurate computations of the laminar flow past a square cylinder based on two different methods: Lattice-Boltzmann and finite-volume, Int J Heat Fluid Flow 21 (2000), 186–196.